Toroidal order in metals without local inversion symmetry

Satoru Hayami,[1] Hiroaki Kusunose,[2] and Yukitoshi Motome[1]

[1]*Department of Applied Physics, University of Tokyo, Tokyo 113-8656, Japan*

[2]*Department of Physics, Ehime University, Matsuyama 790-8577, Japan*

Toroidal order, given by a composite of electric and magnetic orders, manifests itself not only in unusual magnetism but also in anomalous transport and magnetoelectric effects. We report our theoretical results on the influence and stability of toroidal order in metals on the basis of a microscopic model. We consider an effective single-band Hubbard-type model with a site-dependent antisymmetric spin-orbit coupling, which is derived from a four-band tight-binding model including atomic spin-orbit coupling, off-site hybridization between orbitals with different parities, and an *odd-parity* crystalline electric field. For this single-band model on a layered honeycomb lattice, we investigate the electronic structure, magnetotransport, and magnetoelectric effect in a toroidal ordered state with a vortexlike magnetic structure. The ferroic order of the microscopic toroidal moments acts as an effective gauge field for electrons, which modulates the electronic band structure with a shift of the band bottom in momentum space. In addition, the site-dependent antisymmetric spin-orbit coupling gives rise to highly anisotropic Hall responses. The most salient feature is two different types of magnetoelectric response: one is a magnetic order with net toroidal magnetization induced by an electric current perpendicular to the planes, and the other is a uniform transverse magnetization induced by an electric current within the planes. We examine the ground state of the effective model by the mean-field approximation, and show that the toroidal order is stabilized by strong electron correlations at low electron density. We also discuss the temperature dependence of the magnetoelectric effects associated with spontaneous toroidal ordering. Implications for experiments are also presented.

I. INTRODUCTION

The magnetoelectric effect, which is a consequence of the interplay between electric and magnetic properties of electrons first proposed by Curie [1], has long been studied extensively in condensed matter physics [2–4]. It is an intriguing phenomenon where magnetization is induced by an electric field and electric polarization is induced by a magnetic field. Recently, it has attracted renewed interest since the discovery of multiferroic materials showing large magnetoelectric responses [5–7]. In these magnetic insulators, both spatial-inversion and time-reversal symmetries are broken by a spontaneous magnetic order, yielding simultaneously uniform electric polarization and magnetization [8–11]. Such multiferroic materials have been intensively studied not only from the viewpoint of fundamental physics but also for potential applications to multifunctional devices [12–16].

Toroidal order is one of the states of matter showing such cross correlations between electric and magnetic responses. A toroidal moment, which is represented by a vector product of electric and magnetic moments, was originally introduced as an anapole moment in the context of parity violation by weak interactions [17]. Recently, toroidal order, a periodic array of toroidal moments in crystals, has gained interest because it leads to exotic phenomena, such as a diamagnetic anomaly and nonreciprocal directional dichroism [18–24], in addition to ordinary magnetoelectric effects.

There are several multiferroic materials which exhibit toroidal order. For instance, Cr_2O_3 shows a toroidal order in the spin-flop phase under a strong magnetic field [25,26]. In the magnetic piezoelectric material $GaFeO_3$, a ferroic toroidal order was detected by resonant magnetoelectric x-ray scattering [27]. $LiCoPO_4$ exhibits a large linear magnetoelectric

effect, and the coexistence of ferrotoroidic and antiferromagnetic domains was observed by optical second-harmonic generation [28]. $Ba_2CoGe_2O_7$ gives rise to a spontaneous toroidal order due to single-ion effects [29]. These findings are thus far restricted to insulators.

Toroidal order can exist also in metallic systems despite the absence of a macroscopic polarization. Their influence on electronic and magnetoelectric properties can be more interesting than in insulators owing to their conducting nature. For instance, recently, an antiferromagnetic metal on a zigzag lattice, which accommodates toroidal order, was shown to exhibit an interesting magnetoelectric response [30]. Nonetheless, toroidal order in metals has not been studied intensively, in particular, from the microscopic point of view. To further stimulate experiments on toroidal ordered systems, it is desired to systematically study how toroidal order affects the electronic structure, transport properties, and magnetoelectric effects. It is also important to examine the stability of toroidal order and to clarify the finite-temperature behavior associated with spontaneous toroidal ordering.

In the present study, we investigate a microscopic model in order to clarify the effect of toroidal ordering in metals. In particular, we examine the effect of spontaneous ferroic ordering of toroidal moments with a focus on the lattice structures on which the spatial-inversion symmetry is preserved globally but broken intrinsically at each magnetic site. We consider a low-energy effective single-band model for a minimal four-band tight-binding model. The site-dependent antisymmetric spin-orbit coupling in the effective model is derived from the atomic spin-orbit coupling, off-site hybridization between orbitals with different parities, and an odd-parity crystalline electric field together with electron-electron interactions. As a typical example, we study the effect of toroidal order

triggered by a vortexlike magnetic order in the effective model on a layered honeycomb lattice. The ferroic ordering of microscopic toroidal moments acts as an effective gauge field, which leads to modulations of the band dispersions with a shift of the band bottom from the Γ point. We find that the toroidal magnetic order plays an important role in the anisotropic magnetotransport and the magnetoelectric effects depending on the direction of the applied electric current. In particular, we elucidate that an out-of-plane electric current induces a vortexlike magnetic order, while an in-plane current yields a transverse uniform magnetization in the plane by canting the underlying vortexlike magnetic order. We discuss such effects from a symmetry point of view. We also provide some implications for experiments on toroidal metals. Although qualitatively similar results were obtained for a related model in a previous study [30], the present work provides a comprehensive analysis focusing on the toroidal ordering. Moreover, investigating the model by a mean-field approximation, we find that such a ferroic toroidal order appears at low temperatures in a wide range of strongly correlated regions for low electron density. We also show the temperature dependence of the anomalous magnetoelectric responses. We find that the longitudinal toroidal response to the current exhibits a broad peak around the critical temperature with a kink at the transition, while the transverse uniform magnetization induced by the current shows order-parameter-like behavior.

The organization of this paper is as follows. In Sec. II, we give a brief review of the microscopic definition and the symmetry analysis of toroidal moments. In Sec. III, we investigate the influence of toroidal ordering in metals. After introducing the lattice structures with local inversion symmetry breaking in Sec. III A, we present a low-energy effective Hamiltonian in Sec. III B. We show how the toroidal order affects the electronic structure, anisotropic magnetotransport, and magnetoelectric effects in Secs. III C, III D, and III E, respectively. In Sec. IV, we examine the stability of the toroidal magnetic order at the level of the mean-field approximation. The results for the ground state and the finite-temperature properties are presented in Secs. IV A and IV B, respectively. Section V is devoted to a summary of the present paper.

II. TOROIDAL MOMENT

In this section, we introduce the toroidal moment from both microscopic and macroscopic points of view. Although these arguments have already been given in the literature, e.g., in Ref. [22], we give a brief summary to make the present paper self-contained and to understand the microscopic results in the following sections.

First, we discuss the microscopic origin of the toroidal moment. In general, magnetic and toroidal multipoles appear in the multipole expansion of an electromagnetic vector potential,

$$A = \sum_{lm} \sqrt{\frac{4\pi(l+1)}{2l+1}} \frac{1}{r^{l+1}}$$
$$\times \left(\frac{i}{\sqrt{l}} M_{lm} Y_{lm}^l - \frac{\sqrt{2l+1}}{r} T_{lm} Y_{lm}^{l+1} \right), \quad (1)$$
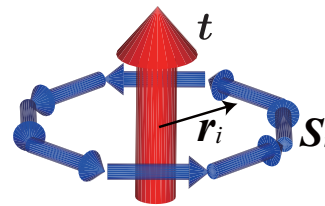

FIG. 1. (Color online) Schematic picture of the toroidal moment, which is defined by the vector product of the position from the inversion center and the magnetic moment. See Eq. (3).

where $Y_{lm}^{l'}$ represents the vector spherical harmonics [31–33]; l and m are the azimuthal and magnetic quantum numbers, respectively, and $l' = l, l \pm 1$. $Y_{lm}^{l'}$ has parity $(-1)^{l'}$ under spatial inversion. Since A is a polar vector with odd time-reversal symmetry, M_{lm} in the first term of Eq. (1) represents the magnetic multipoles (axial tensor) and T_{lm} in the second term the toroidal multipoles (polar tensor). Thus, the even-rank tensor M_{lm} and the odd-rank tensor T_{lm} become active only when both spatial-inversion and time-reversal symmetries are broken. The toroidal moment t appears in the lowest-rank ($l = 1$) contribution in the latter term [18,34,35], which is written in the form

$$t = \frac{1}{6c} \sum_i r_i \times (r_i \times j_i). \quad (2)$$

Here, r_i and j_i are the position vector and the classical circular electric current at r_i, respectively. When there is an internal magnetic field caused by spins instead of the electric current, the toroidal moment is expressed in terms of the localized spin S_i as

$$t = \frac{g\mu_B}{2} \sum_i r_i \times S_i, \quad (3)$$

where g is the g factor and μ_B is the Bohr magneton. This definition indicates that the toroidal moment is represented by the sum of vector products of the position vector and localized spin, as schematically shown in Fig. 1. We note that there is an ambiguity in the definitions in Eqs. (2) and (3) depending on the choice of the origin for r_i [22].

The toroidal moment t appears in the Hamiltonian under an inhomogeneous magnetic field $H(r)$: the Hamiltonian can be expanded at some point $r = 0$ in terms of field gradients as

$$\mathcal{H}_{\text{ext}} = -m \cdot H(0) - t \cdot [\nabla \times H]_{r=0}$$
$$- q_{\mu\nu}(\partial_\mu H_\nu + \partial_\nu H_\mu)_{r=0} + \cdots, \quad (4)$$

where m and $q_{\mu\nu}$ are the magnetic dipole and quadrupole moments, respectively ($\mu, \nu = x, y, z$). The repeated greek indices are implicitly summed over hereafter. Equation (4) indicates that the toroidal moment t couples to the curl of magnetic field, that is, the electric current.

Next, we describe macroscopic responses of the toroidal moment to electromagnetic fields [3,34]. Let us consider an expansion of the free energy with respect to the electric field E and the magnetic field H up to the second order [3]. It is given by

$$F(E,H) = F_0 - \frac{\varepsilon_{\mu\nu} E_\mu E_\nu}{8\pi} - \frac{\mu_{\mu\nu} H_\mu H_\nu}{8\pi} - \alpha_{\mu\nu} E_\mu H_\nu, \quad (5)$$

where F_0 is the free energy in the absence of the electric and magnetic fields; $\varepsilon_{\mu\nu}$, $\mu_{\mu\nu}$, and $\alpha_{\mu\nu}$ are the dielectric permittivity, magnetic permeability, and magnetoelectric tensor, respectively. Equation (5) is useful to discuss the magnetoelectric responses macroscopically. In fact, $\alpha_{\mu\nu}$ in the last term is related to linear magnetoelectric responses, and it is nonzero only when both global spatial-inversion and time-reversal symmetries are broken. The magnetoelectric contribution in the last term can be divided into three terms:

$$- a(\boldsymbol{E} \cdot \boldsymbol{H}) - \boldsymbol{T} \cdot (\boldsymbol{E} \times \boldsymbol{H}) - Q_{\mu\nu}(E_\mu H_\nu + E_\nu H_\mu), \quad (6)$$

where the coefficients of the first, second, and third terms represent the magnetic flux (pseudoscalar), toroidal magnetization $\boldsymbol{T}$ (polar vector), and magnetic quadrupole (symmetric traceless pseudotensor). Thus, the antisymmetric components of the magnetoelectric tensor $\alpha_{\mu\nu}$ correspond to the toroidal magnetization, which is defined as the toroidal moment per unit volume.

The linear magnetoelectric effect caused by toroidal ordering is understood from Eq. (6) [21]. Namely, the second term implies the relations

$$\boldsymbol{P} \propto -\boldsymbol{T} \times \boldsymbol{H}, \quad \boldsymbol{M} \propto \boldsymbol{T} \times \boldsymbol{E}, \quad (7)$$

where $\boldsymbol{P}$ and $\boldsymbol{M}$ are the electric polarization and magnetization, respectively. These indicate that the electric polarization (magnetization) is induced in the direction perpendicular to both the toroidal magnetization and the magnetic (electric) field.

III. TOROIDAL ORDERING IN METALS

Here, we examine the nature of toroidal ordered states in crystals. First, we introduce lattice structures with local inversion symmetry breaking in Sec. III A. Next, we present a minimal low-energy Hamiltonian including the effect of the site-dependent antisymmetric spin-orbit coupling in Sec. III B. By analyzing the effective Hamiltonian on a layered honeycomb lattice, we investigate the influence of toroidal ordering on the electronic structure in Sec. III C, magnetotransport in Sec. III D, and the magnetoelectric effect in Sec. III E.

A. Lattices with local inversion symmetry breaking

A minimal ingredient for activating a toroidal moment is spatial-inversion symmetry breaking at each magnetic site. In such situation, an odd-parity crystalline electric field is present at the magnetic sites, which mixes orbitals with different parities. Such local parity mixing together with the atomic spin-orbit coupling plays an important role in realizing toroidal ordering in metals, as we will see in the following sections.

In order to demonstrate the above scenario, we focus on lattice structures in which the inversion symmetry is broken locally at each site but the global inversion symmetry is preserved at off-site positions. There are several lattices with such local inversion symmetry breaking; for instance, a one-dimensional (1D) zigzag chain [Fig. 2(a)], a two-dimensional honeycomb lattice [Fig. 2(b)], a 1/5-depleted square lattice [Fig. 2(c)], and a three-dimensional (3D) diamond lattice. On these lattices, the spatial-inversion symmetry is broken at the
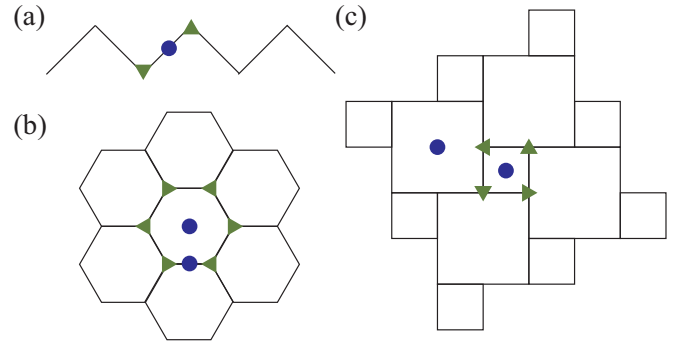

FIG. 2. (Color online) Schematic pictures of lattice structures with local inversion symmetry breaking: (a) One-dimensional zigzag chain, (b) honeycomb lattice, and (c) 1/5-depleted square lattice. Circles indicate the inversion centers, while triangles represent the lattice sites at which the inversion symmetry is broken.

lattice sites (triangles in Fig. 2), although it is preserved at the centers of bonds or plaquettes (circles).

B. Effective single-band model

In order to describe the origins of the essential ingredients for a minimal tight-binding model, we start from a generic four-band model with local parity mixing. Following the procedure given in the Appendix, we obtain an effective single-band model, which will mainly be examined in the following sections.

The Hamiltonian for the generic four-band model is given by

$$\mathcal{H}_{\text{4 band}} = \mathcal{H}_{\text{kin}} + \mathcal{H}_{\text{hyb}} + \mathcal{H}_{\text{o-CEF}} + \mathcal{H}_{\text{LS}} + \mathcal{H}_{\text{int}}, \quad (8)$$

where

$$\mathcal{H}_{\text{kin}} = -\sum_{i,j} \sum_{\alpha=s,p_x,p_y,p_z} \sum_\sigma \left(\tilde{t}_{ij}^\alpha \tilde{c}_{i\alpha\sigma}^\dagger \tilde{c}_{j\alpha\sigma} + \text{H.c.} \right), \quad (9)$$

$$\mathcal{H}_{\text{hyb}} = -\sum_{\langle i,j \rangle} \sum_{\alpha=p_x,p_y,p_z} \sum_\sigma \left(\tilde{V}_{ij}^\alpha \tilde{c}_{is\sigma}^\dagger \tilde{c}_{j\alpha\sigma} + \text{H.c.} \right), \quad (10)$$

$$\mathcal{H}_{\text{o-CEF}} = \sum_i \sum_{\alpha=p_x,p_y,p_z} \sum_\sigma (\tilde{D}_i^\alpha \tilde{c}_{is\sigma}^\dagger \tilde{c}_{i\alpha\sigma} + \text{H.c.}), \quad (11)$$

$$\mathcal{H}_{\text{LS}} = \frac{\lambda}{2} \sum_i \sum_{\alpha,\beta=p_x,p_y,p_z} \sum_{\sigma,\sigma'} \tilde{c}_{i\alpha\sigma}^\dagger \tilde{H}_{\text{LS}} \tilde{c}_{i\beta\sigma'}, \quad (12)$$

$$\mathcal{H}_{\text{int}} = \sum_i \sum_{\alpha\beta\alpha'\beta'} \sum_{\sigma\sigma'} U_{\alpha\beta\alpha'\beta'} \tilde{c}_{i\alpha\sigma}^\dagger \tilde{c}_{i\beta\sigma'}^\dagger \tilde{c}_{i\beta'\sigma'} \tilde{c}_{i\alpha'\sigma}. \quad (13)$$

Here, $\tilde{c}_{i\alpha\sigma}^\dagger$ ($\tilde{c}_{i\alpha\sigma}$) is the creation (annihilation) operator of a conduction electron with orbital α and spin σ at site i; we consider four orbitals, i.e., an "s-type" orbital with the angular momentum $l = 0$ (even parity) and three "p-type" orbitals with $l = 1$ (odd parity). This is a minimum set of orbitals for describing parity mixing. Equation (9) represents the kinetic energy of the conduction electrons; the sum is limited to on-site and nearest-neighbor sites. The on-site part describes the atomic energy, which is set as $\tilde{t}_{ii}^s = \tilde{E}^s$ and $\tilde{t}_{ii}^{\alpha=p_x,p_y,p_z} = 0$. Equation (10) describes the off-site hybridization between s

and p orbitals; the sum $\langle i,j \rangle$ is taken for the nearest-neighbor sites, and $\tilde{V}_{ij}^{\alpha}$ depends on the p orbital as well as the bond direction. Equation (11) denotes the odd-parity crystalline electric field; $\tilde{D}_i^{\alpha}$ depends on both site and orbital. Note that $\tilde{D}_i^{\alpha}$ is nonzero only in the absence of local inversion symmetry, while $\tilde{V}_{ij}^{\alpha}$ is always present even with local inversion symmetry. We note that both $\tilde{V}_{ij}^{\alpha}$ and $\tilde{D}_i^{\alpha}$ are indispensable to obtain the site-dependent antisymmetric spin-orbit coupling in the effective model (see the Appendix). Equation (12) represents the atomic spin-orbit coupling for p orbitals with $l=1$: $\tilde{H}_{\mathrm{LS}}$ is the 6×6 matrix given by

$$\tilde{H}_{\mathrm{LS}} = \begin{pmatrix} 0 & -i\sigma^z & i\sigma^y \\ i\sigma^z & 0 & -i\sigma^x \\ -i\sigma^y & i\sigma^x & 0 \end{pmatrix}, \qquad (14)$$

where σ^{μ} is the μ component of the Pauli matrix for spin. Finally, Eq. (13) is a general form of the on-site Coulomb interactions. Here, we take account of only the intraorbital components for simplicity, i.e., $U_{\alpha\beta\alpha'\beta'} = (U/2)\delta_{\alpha\beta}\delta_{\alpha'\beta'}\delta_{\alpha\alpha'}$ ($\delta_{\alpha\beta}$ is the Kronecker delta).

We treat the interaction term at the level of a mean-field approximation to allow magnetic solutions. The mean-field form is given by

$$\mathcal{H}_{\mathrm{int}}^{\mathrm{MF}} = -\sum_{i}\sum_{\alpha=s,p_x,p_y,p_z} \tilde{M}_i^{\alpha} \cdot \tilde{s}_i^{\alpha}, \qquad (15)$$

where the mean field $\tilde{M}_i^{\alpha} = 2U\tilde{m}_i^{\alpha}$ and the magnetic moment $\tilde{m}_i^{\alpha} = \langle \tilde{s}_i^{\alpha} \rangle = \langle \sum_{\sigma\sigma'} \tilde{c}_{i\alpha\sigma}^{\dagger}(\boldsymbol{\sigma}_{\sigma\sigma'}/2)\tilde{c}_{i\alpha\sigma'} \rangle$. We omit a constant from the mean-field decoupling here and in Sec. III.

In the present study, we focus on a 3D system composed of weakly coupled uniform 1D chains running in the z direction. By several simplifications in the limit of strong spin-orbit coupling (see the Appendix), we arrive at an effective single-band model, whose Hamiltonian is given by

$$\mathcal{H}^{\mathrm{MF}} = -t \sum_{\langle i,j \rangle}\sum_{\sigma} (c_{i\sigma}^{\dagger}c_{j\sigma} + \mathrm{H.c.}) \\ + 2\sum_{i}(\boldsymbol{s}_i \times \boldsymbol{D}_i)^z - \sum_{i}\boldsymbol{M}_i \cdot \boldsymbol{s}_i. \qquad (16)$$

Here, $c_{i\sigma}^{\dagger}$ ($c_{i\sigma}$) is the creation (annihilation) operator of a conduction electron in the effective single band at site i and quasispin σ, which distinguishes the time-reversal pair states; $\boldsymbol{s}_i = \sum_{\sigma,\sigma'} c_{i\sigma}^{\dagger}(\boldsymbol{\sigma}_{\sigma\sigma'}/2)c_{i\sigma'}$. The first term is the kinetic energy of the electrons with a renormalized hopping t; we assume isotropic hopping for the in-chain and out-of-chain directions for simplicity, as the anisotropic case gives qualitatively the same results. Hereafter, we set $t=1$ as the energy unit. The second term represents the site-dependent antisymmetric spin-orbit coupling, in which $\boldsymbol{D}_i$ is a site-dependent antisymmetric vector with respect to k_z, originating from the odd-parity crystalline electric field $\tilde{D}_i^{\alpha}$, the off-site hybridization $\tilde{V}_{ij}^{\alpha}$, and the atomic spin-orbit coupling λ [see Eq. (A7) in the Appendix]. The third term in Eq. (16) describes the mean-field form of the Coulomb interaction between electrons; $\boldsymbol{M}_i = 2U\boldsymbol{m}_i$, where $\boldsymbol{m}_i = \langle \boldsymbol{s}_i \rangle$ is the magnetic moment at site i.

In the following, we consider the model in Eq. (16) on a stacked honeycomb lattice, as shown in Fig. 3. We take the lattice constants $a=c=1$. Extensions to other lattices
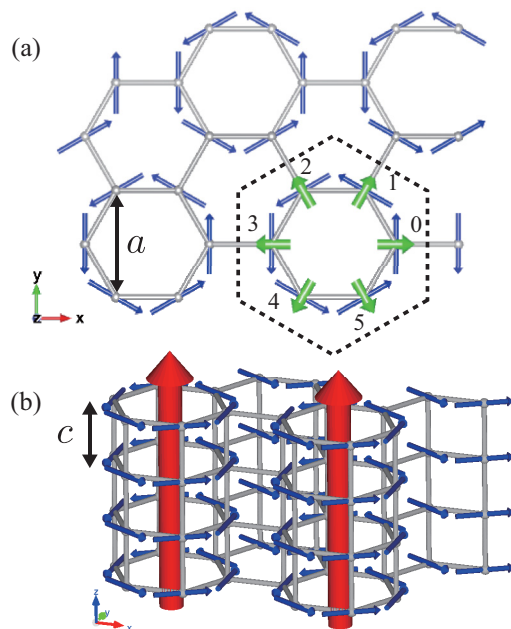

FIG. 3. (Color online) (a) Schematic picture of a projection of the layered honeycomb lattice onto the xy plane. The thin (blue) arrows show the magnetic pattern assumed in the toroidal ordered state [Eq. (18)], and the thick (green) arrows indicate the specific directions of the odd-parity crystalline electric field [Eq. (17)]. The dashed hexagon represents the six-sublattice unit cell with the sublattice indices ($l=0,1,\ldots,5$). a is the lattice constant in the xy plane. (b) Schematic picture of the layered honeycomb lattice. The red arrows in the z direction represent the toroidal magnetizations. c is the lattice constant in the z direction.

with local inversion symmetry breaking are straightforward. For the present stacked honeycomb-lattice case, we assume the presence of $\boldsymbol{D}_i$ in a six-sublattice form with the specific directions in the xy plane as shown by the thick arrows in Fig. 3(a). We also assume that the same patterns of $\boldsymbol{D}_i$ are stacked along the z direction. The form in the six-site sublattice is represented by

$$\boldsymbol{D}_l = D \sin k_z \left(\cos\frac{\pi}{3}l, \ \sin\frac{\pi}{3}l, 0 \right), \qquad (17)$$

where l is the sublattice index ($l=0,1,\ldots,5$) and D is a parameter to control the magnitude of the antisymmetric spin-orbit coupling. It is worth noting that the factor of $\sin k_z$ always enters into $\boldsymbol{D}_l$ in quasi-1D systems; see the derivation in the Appendix.

Furthermore, in the following sections, we assume a six-sublattice vortex-type magnetic order as shown in Fig. 3(a) in a mean-field form. We call it the toroidal magnetic order hereafter. Specifically, the mean field for the toroidal magnetic order is given by

$$\boldsymbol{M}_l = M_T \left(-\sin\frac{\pi}{3}l, \ \cos\frac{\pi}{3}l, 0 \right). \qquad (18)$$

Here, M_T is a measure of the mean field for the toroidal magnetic order, which is treated as a free parameter throughout in this section, while it will be determined by solving the self-consistent equations in Sec. IV. We note that a similar magnetic pattern was indeed observed in the partially ordered

state below 20 K in a uranium compound UNi$_4$B [36]. We will remark on this point in Sec. V.

Since D_l plays the role of a local electric field and $D_l \perp M_l$ at each site, the toroidal magnetic order M_l must accompany a ferroic order of toroidal moments, $T \propto D_l \times M_l = (0,0,DM_T \sin k_z)$, as shown in Fig. 3(b). In other words, even if a macroscopic polarization is absent, a spontaneous toroidal order can be realized by specific magnetic ordering with underlying local inversion symmetry breaking.

C. Electronic structure

Let us first discuss the electronic structure of the model in Eq. (16) with Eqs. (17) and (18). Figure 4 shows the band structures in the k_z direction from $k = (0,0,-\pi)$ to $(0,0,\pi)$ for several values of D and M_T.

Figure 4(a) shows the band structure in the paramagnetic state ($M_T = 0$) at $D = 0$, where both spatial-inversion and time-reversal symmetries are preserved. In this case, there are three bands; the top and bottom bands are each doubly degenerate, while the middle one is eightfold degenerate. When only the time-reversal symmetry is broken by the toroidal magnetic order $M_T \neq 0$ at $D = 0$, the bands are split into two bunches depending on the spins parallel or antiparallel to the mean field M_l. Each bunch consists of three bands, each of which remains doubly degenerate due to the global inversion symmetry: the band dispersions satisfy the relation $\epsilon_\sigma(k) = \epsilon_\sigma(-k)$. Meanwhile, when D is nonzero representing local inversion symmetry breaking and the system is in the paramagnetic state ($M_T = 0$), the antisymmetric spin splitting of the bands occurs, as shown in Fig. 4(c). Here, the time-reversal symmetry ensures that $\epsilon_\sigma(k) = \epsilon_{-\sigma}(-k)$. It should

be noted however that each band is still doubly degenerate as the global inversion symmetry remains: $\epsilon_\sigma(k) = \epsilon_\sigma(-k)$. This is different from the case with an ordinary antisymmetric spin-orbit coupling such as that of Rashba type where *global* inversion symmetry is broken.

What happens when the system exhibits toroidal order, i.e., for $M_T \neq 0$ and $D \neq 0$? In this case, both spatial-inversion $\mathcal{P}$ and time-reversal $\mathcal{T}$ symmetries are broken. Each band, however, retains twofold degeneracy owing to the combined $\mathcal{PT}$ symmetry, which ensures that $\epsilon_\sigma(k) = \epsilon_{-\sigma}(k)$. However, there is no guarantee that the energy at k is degenerate with that at $-k$. In fact, the resultant band structure consists of six bands, each doubly degenerate, with a shift of the band bottom from the Γ point, as shown in Fig. 4(d).

The modulation of the bands with a shift of the band bottom is understood in the single-chain limit as follows. The Hamiltonian for the single chain is given by a simple form of the 2×2 matrix:

$$\mathcal{H}_{1D}^{MF} = \begin{pmatrix} -2t\cos k_z & iD^- + M^-/2 \\ -iD^+ + M^+/2 & -2t\cos k_z \end{pmatrix}, \quad (19)$$

where $D^\pm = (D^x \pm iD^y)\sin k_z$ and $M^\pm = M^x \pm iM^y$. Here, $D = (D^x, D^y, 0)\sin k_z$ and $M = (M^x, M^y, 0)$. See also Eq. (A5) in the Appendix. The energy spectrum of this Hamiltonian is given by

$$\epsilon(k_z) = -2t\cos k_z \pm \sqrt{D^2 + M^2/4 - (D \times M)^z}. \quad (20)$$

As D is proportional to $\sin k_z$ [see Eq. (17)] and the last term in the square root is linear in D, a shift of the band bottom occurs when $D \times M \neq 0$, which is proportional to the toroidal magnetization.

The results indicate that the toroidal magnetization acts as an effective gauge field for conduction electrons. The shifted band structure, however, does not generate spontaneous electric current in the equilibrium state due to the gauge invariance [30,37]. The asymmetric band structure can be detected in principle by experiments, such as angle-resolved photo-emission spectroscopy. We expect that the unusual band deformation may become the origin of nonlinear optical effects, such as nonreciprocal directional dichroism [38].

We note that the system has particle-hole symmetry. Indeed, the Hamiltonian in Eq. (16) is unchanged by the particle-hole transformation $(c_{l\sigma}, c_{l\sigma}^\dagger) \rightarrow (-1)^l(d_{l\sigma}^\dagger, d_{l\sigma})$ with a shift of k_z by π and $M_l \rightarrow -M_l$. This symmetry is also seen in the band structure in Fig. 4; the band dispersions satisfy $\epsilon_\sigma(k_z) = -\epsilon_{-\sigma}(\pi - k_z)$.

D. Magnetotransport

We here discuss magnetotransport coefficients for the model in Eq. (16) with Eqs. (17) and (18). We calculate the conductivity tensor in terms of the current-current correlation by the standard Kubo formula as

$$\sigma_{\mu\nu} = \frac{e^2}{\hbar} \frac{1}{iV} \sum_{m,n,k} \frac{f(\epsilon_{nk}) - f(\epsilon_{mk})}{\epsilon_{nk} - \epsilon_{mk}} \frac{J_{\mu,k}^{nm} J_{\nu,k}^{mn}}{\epsilon_{nk} - \epsilon_{mk} + i\delta}, \quad (21)$$

where V is the system volume, $f(\epsilon)$ is the Fermi distribution function, $J_{\mu,k}^{nm} = \langle nk|J_\mu|mk\rangle$ [J_μ is the current operator in the direction $\mu = (x,y,z)$], and ϵ_{mk} and $|mk\rangle$ are the eigenvalue
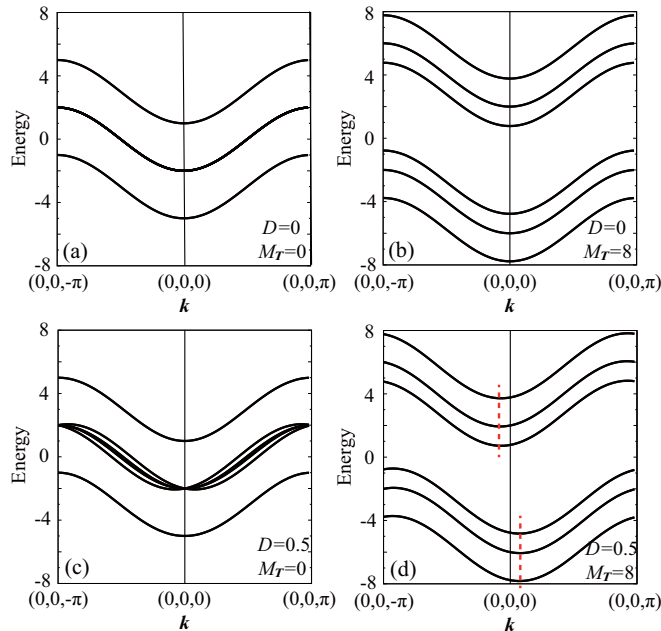

FIG. 4. (Color online) Energy dispersion along the k_z direction of the Hamiltonian in Eq. (16) with Eqs. (17) and (18) for (a) $D = 0$, $M_T = 0$, (b) $D = 0$, $M_T = 8$, (c) $D = 0.5$, $M_T = 0$, and (d) $D = 0.5$, $M_T = 8$. The dashed red lines in (d) indicate the band bottoms in the k_z direction.
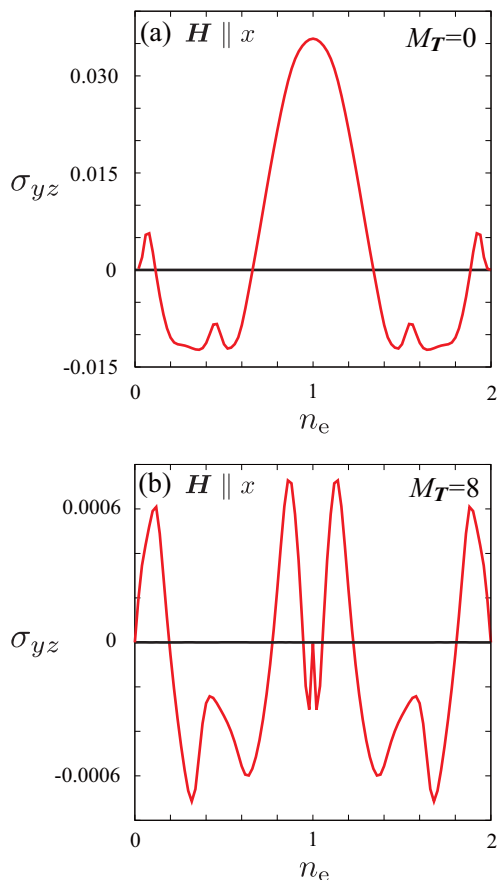
FIG. 5. (Color online) Electron density dependence of the Hall conductivity for (a) $M_T = 0$ and (b) $M_T = 8$. The data are obtained at $D = 0.5$ in the magnetic field $H = 0.5$ applied in the x direction. We take the broadening factor $\delta = 0.01$ and temperature $T = 0.1$.

and eigenstate of $\mathcal{H}^{\mathrm{MF}}$ with the Zeeman term (see below). Here, m and n are the band indices. We take $e^2/h = 1$ (e is the elementary charge and h is the Planck constant), a broadening factor $\delta = 0.01$, and temperature $T = 0.1$. The summation of $\boldsymbol{k}$ is taken over the folded Brillouin zone in the magnetically ordered state.

Figure 5 shows the Hall conductivity σ_{yz} as a function of the electron density $n_{\mathrm{e}} = (1/N) \sum_{i\sigma} \langle c_{i\sigma}^\dagger c_{i\sigma} \rangle$, where N is the total number of sites. The results are obtained for $D = 0.5$ in a magnetic field applied in the x direction; here, we added the Zeeman term $\mathcal{H}_{\mathrm{Z}} = -H \sum_i s_i^x$ to the Hamiltonian $\mathcal{H}^{\mathrm{MF}}$ in Eq. (16). The results are symmetric with respect to $n_{\mathrm{e}} = 1$ because of the particle-hole symmetry discussed at the end of the previous section.

Figure 5(a) shows the Hall conductivity in the absence of the toroidal magnetic order $M_T = 0$. The sign and magnitude of the Hall conductivity depend on the electron density n_{e}, reflecting the nature of the carriers near the Fermi level. It is highly anisotropic; only the $\sigma_{yz(xz)}$ component becomes nonzero in the magnetic field applied in the x (y) direction. This is a consequence of the presence of the (site-dependent) antisymmetric spin-orbit coupling. Indeed, $\sigma_{\mu\nu}$ disappears if we take $D = 0$. The toroidal magnetic order affects significantly the behavior of the Hall conductivity, as shown in

Fig. 5(b) for $M_T = 8$. Although the anisotropy of $\sigma_{\mu\nu}$ does not change in the presence of M_T, the Hall conductivity is strongly suppressed. As will be shown in the next section, M_T has strong temperature dependence in the ordered state, and hence $\sigma_{\mu\nu}$ should exhibit strong suppression with decrease of temperature.

E. Magnetoelectric effect

Now let us discuss magnetoelectric effects in the toroidal ordered state. We compute the linear response function in terms of the correlation between the (toroidal) magnetization and an electric current caused by an electric field in the form

$$K_{\mu\nu} = \frac{g\mu_{\mathrm{B}}}{2} \frac{e}{\hbar} \frac{1}{iV} \sum_{m,n,\boldsymbol{k}} \frac{f(\epsilon_{n\boldsymbol{k}}) - f(\epsilon_{m\boldsymbol{k}})}{\epsilon_{n\boldsymbol{k}} - \epsilon_{m\boldsymbol{k}}} \frac{\sigma_{\mu,\boldsymbol{k}}^{nm} J_{\nu,\boldsymbol{k}}^{mn}}{\epsilon_{n\boldsymbol{k}} - \epsilon_{m\boldsymbol{k}} + i\delta}, \tag{22}$$

where $\sigma_{\mu,\boldsymbol{k}}^{nm} = \langle n\boldsymbol{k}|\sigma_\mu|m\boldsymbol{k}\rangle$. We take $g\mu_{\mathrm{B}} e/2h = 1$. In the following, we discuss two different types of magnetoelectric effects: one is the toroidal magnetic response ($\mu = \boldsymbol{T}$) to an electric current, and the other is the uniform magnetization ($\mu = x, y, z$) induced by an electric current.

1. Longitudinal toroidal magnetization caused by electric current

First, we focus on the toroidal magnetic response to an electric current. Here, we consider $\sigma_{T,\boldsymbol{k}}^{nm}$ in Eq. (22) as the toroidal magnetic order in Eq. (18). Hence, for instance, K_{T_z} is the coefficient for the toroidal magnetic order induced by the electric current in the z direction. Among K_{T_ν}, only K_{T_z} becomes nonzero, as will be discussed in Sec. III E 3 and shown in the table in Fig. 7.

Figure 6(a) shows K_{T_z} as a function of the electron density n_{e}. K_{T_z} becomes nonzero in the entire region of n_{e} except for the insulating cases at $n_{\mathrm{e}} = 0$, 1, and 2. Note that K_{T_z} is antisymmetric with respect to $n_{\mathrm{e}} = 1$ because of the sign change of the magnetic moment in the particle-hole transformation discussed in Sec. III C. The result indicates that toroidal magnetization can be induced by an electric current in the z direction. This provides the possibility in experiments of aligning the toroidal domains by cooling the system in a current flow perpendicular to the planes.

Although the toroidal magnetic response shows complicated behavior depending on both n_{e} and M_T, it tends to be smaller for larger M_T. This tendency is clearly seen in the low- and high-density regions where the Fermi surface has a simple shape. The inset of Fig. 6(a) displays the behavior of K_{T_z} at low density $n_{\mathrm{e}} = 0.1$ as a function of M_T; the toroidal magnetic response is largest at $M_T = 0$, and is suppressed as M_T increases. This susceptibilitylike behavior suggests that K_{T_z} as a function of temperature becomes largest near the critical temperature for the toroidal ordered state, as long as the transition is of second order. Indeed, we will see such behavior in the mean-field calculation in Sec. IV B.

We note that K_{T_z} substantially depends on the broadening factor δ in Eq. (22). This indicates that this quantity has a dominant contribution from the intraband components with $m = n$ in Eq. (22).
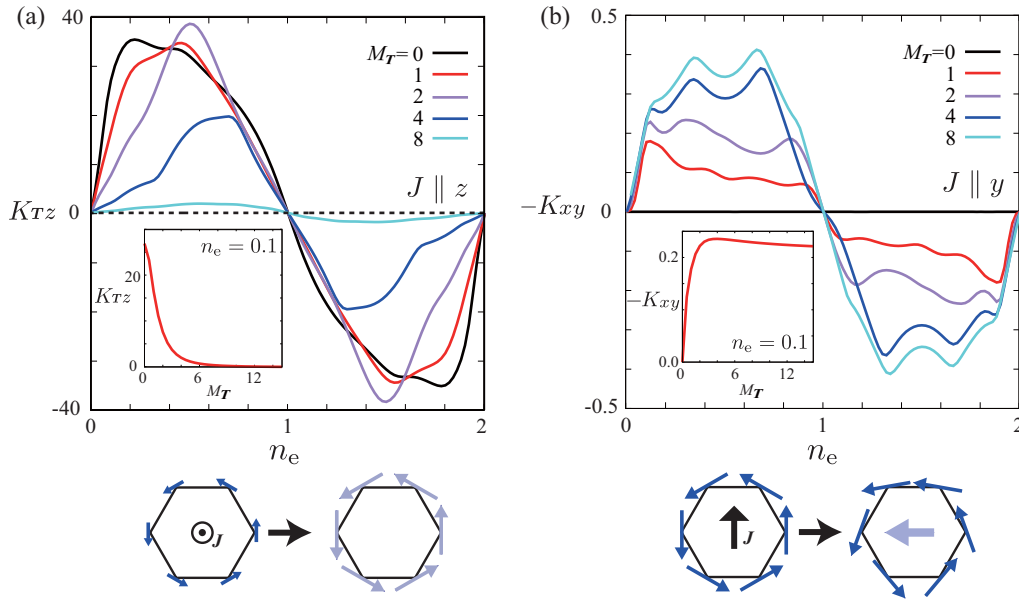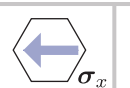
FIG. 6. (Color online) Electron density dependence of (a) the toroidal-current correlation K_{T_z} and (b) the magnetization-current correlation K_{xy}. The insets of (a) and (b) show their M_T dependences at $n_e = 0.1$. The data are obtained for $D = 0.5$, $\delta = 0.01$, and $T = 0.1$. Schematic pictures for the magnetoelectric responses are shown in the bottom panels. In each panel, the left and right pictures show the alignment of the magnetic moments before and after the electric current is applied. In the rightmost one, the arrow in the center of hexagon indicates a net uniform magnetization induced by the electric current.

2. Transverse magnetization caused by electric current

Next, we discuss another magnetoelectric effect, the transverse magnetic response to an electric current. Here, we consider $\sigma_{\mu,k}^{nm}$ with $\mu = x, y, z$ in Eq. (22). For instance, K_{xy} is the coefficient for the uniform magnetization in the x direction induced by the electric current in the y direction. Among $K_{\mu\nu}$, only the transverse components within the plane, i.e., K_{xy} and K_{yx} become nonzero, and they satisfy the antisymmetric relation $K_{xy} = -K_{yx}$ deduced from Eq. (6); see also the discussion about the table in Fig. 7 in Sec. III E 3.
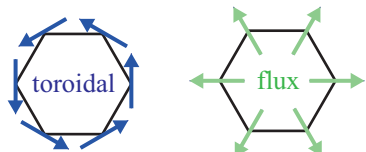

FIG. 7. (Color online) Summary of the magnetoelectric effects under toroidal or flux orders. In the table, "toroidal" and "flux" indicate the underlying magnetic orders for which the magnetic response in the top row is induced by the electric current in the left column. "Any" represents paramagnetic or any magnetically ordered state, including the toroidal and flux orders. Schematic pictures of the toroidal and flux orders are shown at the bottom; the arrows indicate the magnetic moments.

Figure 6(b) shows the result for K_{xy} as a function of the electron density n_e. Similarly to K_{T_z} in Fig. 6(a), K_{xy} shows a nonzero value in the entire region of n_e, except for the insulating cases at $n_e = 0$, 1, and 2, and it is antisymmetric with respect to $n_e = 1$. The result indicates that a uniform magnetization can be induced by an electric current when toroidal order is present ($M_T \neq 0$). This is considered as a multiferroic response in metals with simultaneous breaking of spatial-inversion and time-reversal symmetry. Experimentally, a nonzero value of $K_{xy} = -K_{yx}$ is an indication of toroidal order.

The magnitude of the induced magnetization becomes larger for larger M_T, in contrast to the toroidal magnetic response K_{T_z} in Fig. 6(a). $K_{xy} = 0$ for $M_T = 0$ is due to the presence of time-reversal symmetry, and K_{xy} increases with increase of M_T for small M_T and it almost saturates for large M_T, as shown in the inset of Fig. 6(b). In contrast to K_{T_z}, K_{xy} weakly depends on δ, indicating that a dominant contribution comes from the interband components in Eq. (22).

3. Summary of magnetoelectric effects

We summarize the results of magnetoelectric effects obtained for the model in Eq. (16) with Eqs. (17) and (18). Figure 7 shows a table indicating the magnetoelectric effects in terms of the applied electric current (in the left column) and the resultant magnetic response (in the top row). "Toroidal" or "flux" in the table represents the underlying magnetic order. Thus, the magnetoelectric responses in the layered honeycomb lattice are classified according to the applied current direction. This relationship is essentially the same as in the insulating case, where the electric current is replaced by the electric field.

As shown in Sec. III E 1, an electric current in the z direction induces an additional magnitude of the toroidal magnetization

to the underlying magnetic order [Eq. (18)] while preserving the ordering pattern. This is a natural consequence of the coupling between the toroidal moment and the electric current in the second term in Eq. (4) together with the relation $M_l \propto D_l \times T$. As suggested by the coupling term, this magnetoelectric effect is present even in the absence of toroidal order; in fact, the induced magnetization is largest for $M_T = 0$ [see the inset of Fig. 6(a)].

In contrast, by applying the current in the x (y) direction in the toroidal ordered state, uniform magnetization is induced perpendicular to the current direction within the plane, as shown in Sec. III E 2. This is a transverse response of the magnetization to the electric current, described in the second relation in Eq. (7). As suggested by the relation, this magnetoelectric effect becomes nonzero only in the presence of toroidal magnetization [see the inset of Fig. 6(b)]. Thus, the results in the metallic state in our model are consistent with the symmetry analysis in Sec. II. Systematic measurements of these magnetoelectric effects will be useful for detection of toroidal order in metals.

For comparison, we consider the case of a complementary magnetic order, a flux-type order, as shown in the schematic picture in Fig. 7. This is the magnetic order obtained by rotating the magnetic moments in the toroidal ordered state by 90°. Note that, in the flux state, the magnetic moments are parallel to the antisymmetric vector D_i at each site, and hence the toroidal moment vanishes. Although both the spatial-inversion and time-reversal symmetries are broken in this flux state as well, the magnetoelectric response within the xy plane appears in a complementary manner to that for the toroidal ordered state, as shown in the table in Fig. 7; instead of the transverse response in the toroidal case, a longitudinal magnetization is induced by the in-plane current. These are also consistent with the symmetry analysis in Sec. II; the longitudinal response is described by the pseudoscalar term in Eq. (6).

IV. MEAN-FIELD CALCULATIONS

In Sec. III, we simply assumed the toroidal order given by Eq. (18) on the layered honeycomb lattice and discussed the resultant electronic state, transport properties, and magneto-electric effects. Now, we examine when and how such a ferroic toroidal ordered state is realized in the effective single-band model. For that purpose, we restore the Coulomb interaction for the mean-field term in Eq. (16) in the form

$$\mathcal{H} = -t \sum_{\langle i,j \rangle} \sum_{\sigma} (c_{i\sigma}^{\dagger} c_{j\sigma} + \text{H.c.})$$
$$+ 2 \sum_{i} (s_i \times D_i)^z + U \sum_{i} c_{i\uparrow}^{\dagger} c_{i\uparrow} c_{i\downarrow}^{\dagger} c_{i\downarrow}. \quad (23)$$

Here, we apply the standard Hartree-Fock approximation to the Coulomb U term: we decouple the two-body term to a one-body form by introducing the mean fields $\langle c_{i\sigma}^{\dagger} c_{i\sigma'} \rangle$ as

$$c_{i\uparrow}^{\dagger} c_{i\uparrow} c_{i\downarrow}^{\dagger} c_{i\downarrow}$$
$$\sim c_{i\uparrow}^{\dagger} c_{i\uparrow} \langle c_{i\downarrow}^{\dagger} c_{i\downarrow} \rangle + \langle c_{i\uparrow}^{\dagger} c_{i\uparrow} \rangle c_{i\downarrow}^{\dagger} c_{i\downarrow} - \langle c_{i\uparrow}^{\dagger} c_{i\uparrow} \rangle \langle c_{i\downarrow}^{\dagger} c_{i\downarrow} \rangle$$
$$- c_{i\uparrow}^{\dagger} c_{i\downarrow} \langle c_{i\downarrow}^{\dagger} c_{i\uparrow} \rangle - \langle c_{i\uparrow}^{\dagger} c_{i\downarrow} \rangle c_{i\downarrow}^{\dagger} c_{i\uparrow} + \langle c_{i\uparrow}^{\dagger} c_{i\downarrow} \rangle \langle c_{i\downarrow}^{\dagger} c_{i\uparrow} \rangle, \quad (24)$$

where $\langle \cdots \rangle$ is the statistical average with respect to the one-body Hamiltonian. We assume the mean-field solution in the same six-sublattice form as D_l, but allow arbitrary magnetic and charge patterns within the unit cell (the magnetic moments are assumed to be within the xy plane). Starting from several states with different spin and charge patterns, we determine the mean fields self-consistently by solving the one-body problem by exact diagonalization. In the calculations of the mean fields, we take the sum over 64^3 grid points in the folded Brillouin zone. We determine the phase diagram by comparing the free energies between several converged states with different types of ordering patterns. The physical quantities are calculated from the corresponding eigenvalues and eigenstates. In Sec. IV A, we elucidate the ground-state phase diagram. Finite-temperature properties are discussed in Sec. IV B.

A. Ground state

First, we examine the ground state of the model given by Eq. (23) by changing U and the electron density n_e. Figure 8 shows the ground-state phase diagram obtained by the mean-field calculations at $D = 3$. The result shows that several magnetic states appear in the large-U region. Among them, the toroidal ordered phase is stabilized in the low-density region. This is a metallic state with a shifted band structure
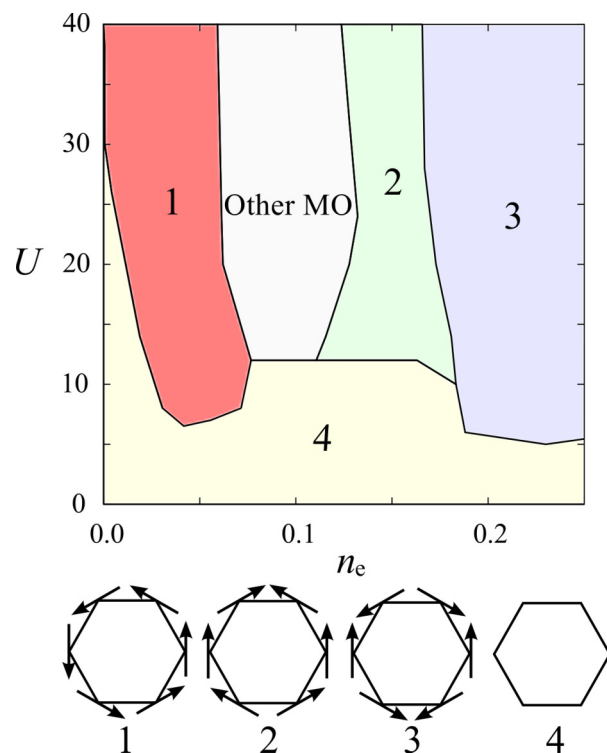

FIG. 8. (Color online) Ground-state phase diagram of the model in Eq. (23) on a layered honeycomb lattice obtained by the mean-field calculations. The data are taken at $D = 3$. Schematic pictures of the ordering patterns are shown in the bottom panel. The arrows represent magnetic moments. "Other MO" represents other complicated magnetically ordered states. Phase 1 corresponds to the toroidal ordered state. There exist no flux-type orders.
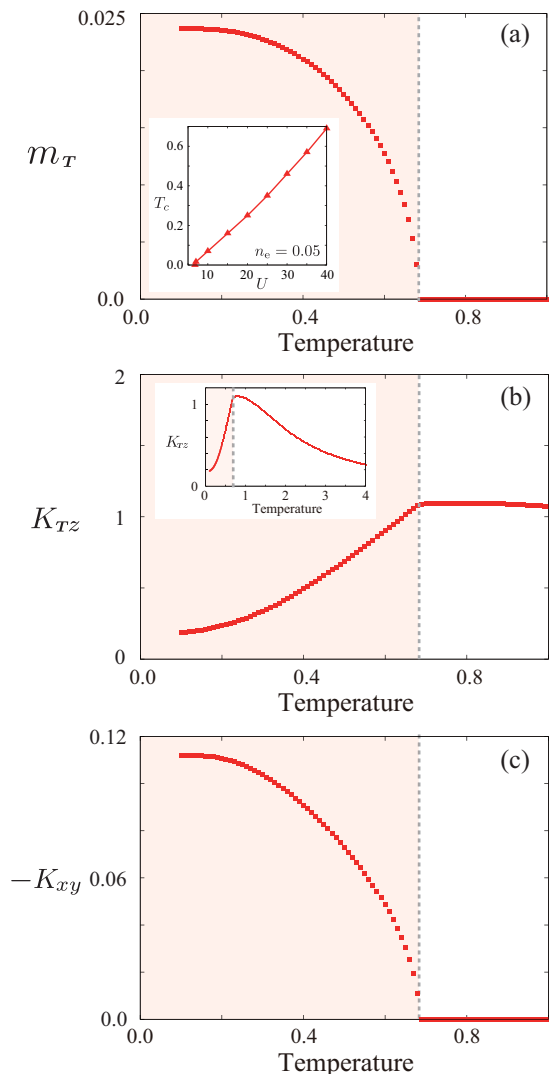
FIG. 9. (Color online) Temperature dependences of (a) the magnitude of the toroidal magnetic moments m_T, (b) K_{Tz}, and (c) K_{xy} at $U = 40$, $D = 3$, and $n_e = 0.05$. The inset of (a) shows the U dependence of T_c for $n_e = 0.05$. K_{Tz} in a broader temperature range is shown in the inset of (b). The shaded temperature region indicates the toroidal ordered phase and the vertical dotted lines show the transition temperature T_c.

and shows magnetoelectric effects as well as magnetotransport phenomena, as shown in Sec. III.

B. Finite temperature

Next, we discuss the finite-temperature properties in toroidal ordering within the mean-field approximation. The parameters are taken at $U = 40$, $D = 3$, and $n_e = 0.05$. Figure 9(a) shows the result for the magnitude of the toroidal magnetic order parameter $m_T = M_T/(2U)$ [see Eq. (18) and Fig. 3]. While increasing temperature, m_T decreases continuously to zero at the critical temperature $T_c \simeq 0.69$; this signals the second-order transition from the low-temperature toroidal ordered state to the high-temperature paramagnetic state. We also show the U dependence of T_c at $n_e = 0.05$ in the inset of Fig. 9(a).

Figures 9(b) and 9(c) show the temperature dependences of the magnetoelectric responses. We use the formula in Eq. (22) with $\delta = 0.1$. Figure 9(b) displays K_{Tz}. The result shows that the magnitude of K_{Tz} becomes largest at $T \simeq T_c$ and rapidly decreases for lower temperatures after showing a kink at T_c [see also the inset in Fig. 9(b)]. The behavior is consistent with that expected from the result of the ground state in the inset of Fig. 6(a): K_{Tz} becomes largest at $M_T = 0$ and decreases as M_T increases. From the result, we conclude that the system exhibits a large toroidal magnetic response at and slightly above the critical temperature. Note that similar behavior was observed in the magnetoresistance in so-called double-exchange systems, such as perovskite manganese oxides [39–42].

On the other hand, as shown in Fig. 9(c), $-K_{xy}$ behaves like the order parameter m_T; it becomes nonzero below T_c and grows rapidly as decreasing temperature. This is also consistent with the expectation from the ground-state calculation shown in the inset of Fig. 6(b).

V. SUMMARY AND CONCLUDING REMARKS

In summary, we have investigated the effect and stability of toroidal order in metals on a lattice without local inversion symmetry. We have introduced an effective single-band Hubbard-type model with a site-dependent antisymmetric spin-orbit coupling, while presenting the detailed derivation from a minimal four-band model. Considering an in-plane vortexlike magnetic order which accommodates a ferroic toroidal order on a stacked honeycomb lattice, we have studied the effect of the toroidal order on the electronic structure, magnetotransport, and magnetoelectric effects. We have explicitly shown in the microscopic model that (i) when the toroidal order is realized, the bottom of the electronic bands shifts in the direction of the toroidal magnetization, (ii) the anisotropic Hall response appears due to the site-dependent antisymmetric spin-orbit coupling, (iii) the system exhibits two different types of magnetoelectric effects: a longitudinal toroidal magnetic response to an electric current in the out-of-plane direction and a transverse uniform magnetization induces by an electric current in the plane. We have also investigated the stability of the toroidal ordered state in the effective model by the mean-field approximation. We have shown that the toroidal ordered state is stabilized in the strongly-correlated region at low electron density. We have also examined the nature of the finite-temperature phase transition for the toroidal ordering and the temperature dependence of the magnetoelectric effects. We have shown that the transition is continuous and that the toroidal magnetic response is maximized around the critical temperature, while the uniform magnetization induced by a current behaves like a toroidal order parameter.

Our results provide a reference for further exploration of toroidal order in metallic magnets. Our model includes the essential ingredients for toroidal ordering; the atomic spin-orbit coupling, off-site hybridizations of different-parity orbitals, an odd-parity crystalline electric field due to the local inversion symmetry breaking of the lattice structure, and electron-electron correlations. A complementary set of measurements of the electronic structure, magnetotransport, and magnetoelectric effects presented here will be useful

for identifying the type of toroidal order. We have also mentioned the possibility of magneto-optical effects, such as a nonreciprocal directional dichroism, and of alignment of toroidal domains by cooling the system in an electric current.

The magnetically ordered state in UNi$_4$B [36,43] could be a candidate for the spontaneous toroidal ordering discussed in the present study. While the lattice structure of this compound is a layered triangular lattice, the system shows partial disorder, which is coexistence between the magnetic order on the honeycomb subnetwork and nonmagnetic sites below 20 K. Interestingly, the magnetic structure on the stacked honeycomb subnetwork is vortexlike, as displayed in Fig. 3. Namely, this compound has the possibility of showing toroidal nature, although the direction and magnitude of the underlying antisymmetric vector $\boldsymbol{D}_l$ remain unknown. Moreover, the electric structure and magnetoelectric effects are not clarified yet, to the best of our knowledge. Further experiments, such as angle-resolved photoemission spectroscopy and measurement of the magnetoelectric tensor, are desirable to examine the possibility of toroidal ordering in this compound. Nonlinear optical effects would be interesting as well.

There are many other candidate materials in which the lattice structure has local inversion symmetry breaking. For instance, in spinels, which consist of a wide range of compounds including both metals and insulators, the spatial-inversion symmetry is broken at the A site; the A sites comprise a diamond lattice, and moreover each A site is located at the center of a ligand tetrahedron where the local inversion symmetry is lost. It is desired to systematically study such materials from the viewpoint of toroidal ordering for further understanding of the exotic electronic and magnetoelectric states.

Finally, let us discuss the possibility of a spontaneous Hall response in the toroidal ordered state. We have discussed the magnetotransport and magnetoelectric effects in the toroidal ordered state in Secs. III D and III E, respectively. By combining these two effects, we deduce that the toroidal order induces an intrinsic Hall response even in the absence of an external magnetic field. Namely, for example, when we apply an electric field in the y direction, a uniform magnetization is induced in the x direction as shown in Sec. III E, which further induces an electric current in the z direction via magnetotransport in Sec. III D. This unusual off-diagonal response in the form of $E_z \propto J_x^2 + J_y^2$ may be useful to characterize the toroidal ordered state in metals. To clarify such an exotic response, it is necessary to perform an analysis beyond the linear response theory used in the present study, which is left for future investigation.

APPENDIX: LOW-ENERGY EFFECTIVE HAMILTONIAN FOR THE FOUR-BAND MODEL

In this Appendix, we present the derivation of the single-band model in Eq. (16). It is derived as a low-energy effective model for the four-band model in Eq. (8) [44]. In the derivation, the four-band model is simplified under the following three assumptions. First, we consider a 3D system composed of uniform 1D chains in the z direction. Namely, we ignore the hopping and hybridization terms between the chains for a while. In this 1D limit, from the symmetry, the only nonzero matrix element in the hybridization term $\mathcal{H}_{\text{hyb}}$ is $\tilde{V}_{ij}^{p_z}$ in the z direction. We hereafter denote $\tilde{t}_{i,i\pm1}^{\alpha} = -t^{\alpha}$ and $\tilde{V}_{i,i\pm1}^{p_z} = \mp t^{sp_z}$ for the nearest neighbors in the z direction. Note that the Fourier transform of $\tilde{V}_{i,i\pm1}^{p_z}$ is written in the form

$$V^{p_z} = -2i\, t^{sp_z} \sin k_z. \tag{A1}$$

Second, we assume that the magnetic moments lie in the xy planes, which are stacked uniformly along the chain. Finally, we take the limit of strong spin-orbit coupling $\lambda \to \infty$. In this limit, the sixfold degeneracy in the p orbitals is split into a $j = 1/2$ doublet and a $j = 3/2$ quartet, as shown in the middle of Fig. 10. We take into account only the lower $j = 1/2$ levels. These three assumptions reduce the Hamiltonian for a 1D chain to the form of

$$\mathcal{H}_{\text{1D}} = \begin{pmatrix} \tilde{\epsilon}^s & -\frac{1}{\sqrt{3}} V^{p_z} & \frac{1}{2}\tilde{M}^- & \frac{1}{\sqrt{3}}\tilde{D}^- \\ -\frac{1}{\sqrt{3}} V^{p_z*} & \tilde{\epsilon}^p - \lambda & -\frac{1}{\sqrt{3}}\tilde{D}^- & \frac{1}{6}\tilde{M}^- \\ \frac{1}{2}\tilde{M}^+ & -\frac{1}{\sqrt{3}}\tilde{D}^+ & \tilde{\epsilon}^s & -\frac{1}{\sqrt{3}} V^{p_z} \\ \frac{1}{\sqrt{3}}\tilde{D}^+ & \frac{1}{6}\tilde{M}^+ & -\frac{1}{\sqrt{3}} V^{p_z*} & \tilde{\epsilon}^p - \lambda \end{pmatrix},$$

$$\tag{A2}$$

where $\tilde{\epsilon}^s(k_z) = \tilde{E}^s - 2t^s \cos k_z$, $\tilde{\epsilon}^p(k_z) = -\frac{2}{3}(t^{p_x} + t^{p_y} + t^{p_z}) \cos k_z$, $\tilde{D}^{\pm} = \tilde{D}^{p_x} \pm i\tilde{D}^{p_y}$, and $\tilde{M}^{\pm} = \tilde{M}^x \pm i\tilde{M}^y$. $\tilde{E}^s = \tilde{t}_{ii}^s$ is the atomic energy level for the s orbital. Here, we dropped the chain index i for simplicity. In Eq. (A2), we take the basis $(\tilde{c}_{s\uparrow}^{\dagger}, \tilde{c}_{p+}^{\dagger}, \tilde{c}_{s\downarrow}^{\dagger}, \tilde{c}_{p-}^{\dagger})$, where

$$\tilde{c}_{p+} = -\frac{1}{\sqrt{3}}(\tilde{c}_{p_x\downarrow} + i\tilde{c}_{p_y\downarrow} + \tilde{c}_{p_z\uparrow}), \tag{A3}$$

$$\tilde{c}_{p-} = \frac{1}{\sqrt{3}}(\tilde{c}_{p_x\uparrow} - i\tilde{c}_{p_y\uparrow} - \tilde{c}_{p_z\downarrow}). \tag{A4}$$

From Eq. (A2), we project out the lowest two levels after taking into account the hybridization between the s and $j = 1/2$ levels, V^{p_z}. Namely, we rewrite the Hamiltonian matrix in Eq. (A2) in terms of the basis which diagonalizes the upper left and lower right 2×2 matrices in Eq. (A2). In the new
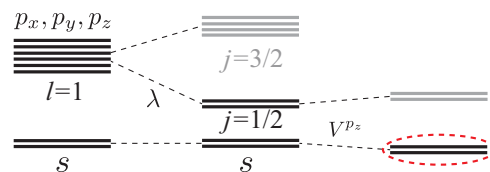

FIG. 10. (Color online) (a) Schematic energy diagram in the derivation of the effective single-band model in Eq. (16) from the four-band model in Eq. (8). The dashed circle represents the energy levels considered in the effective single-band model.

basis, we take into account only the two lower-energy levels; the off-diagonal components between these two levels give the effective antisymmetric spin-orbit coupling and the electron-electron interaction in a mean-field form. Thus, we end up with an effective single-band model, whose Hamiltonian is given by

$$\mathcal{H}_{1D} = \sum_{\sigma} \epsilon(k_z) c_{\sigma}^{\dagger} c_{\sigma} + 2(\boldsymbol{s} \times \boldsymbol{D}(k_z))^z - \boldsymbol{M}(k_z) \cdot \boldsymbol{s}, \quad \text{(A5)}$$

where $(c_{\sigma}, c_{\sigma}^{\dagger})$ is a new basis after considering the effect of the hybridization V^{p_z}, and $\boldsymbol{s} = \sum_{\sigma, \sigma'} c_{\sigma}^{\dagger} (\boldsymbol{\sigma}_{\sigma\sigma'}/2) c_{\sigma}'$. σ is the quasispin distinguishing the two low-energy time-reversal pair states. Here,

$$\epsilon(k_z) = \tilde{\epsilon}_+(k_z) - E(k_z) = \epsilon(-k_z), \quad \text{(A6)}$$

$$\boldsymbol{D}(k_z) = \frac{1}{\sqrt{3}} \frac{\tilde{t}^{sp_z} \sin k_z}{E(k_z)} \tilde{\boldsymbol{D}} = -\boldsymbol{D}(-k_z), \quad \text{(A7)}$$

$$\boldsymbol{M}(k_z) = \frac{2}{3} \left[1 - \frac{1}{2} \frac{\tilde{\epsilon}_-(k_z)}{E(k_z)} \right] \tilde{\boldsymbol{M}} = \boldsymbol{M}(-k_z), \quad \text{(A8)}$$

and

$$E(k_z) = \{ [\tilde{\epsilon}_-(k_z)]^2 + (\tilde{t}^{sp_z} \sin k_z)^2 \}^{1/2}, \quad \text{(A9)}$$

$$\tilde{\epsilon}_{\pm}(k_z) = \frac{1}{2} \{ \tilde{\epsilon}^s(k_z) \pm [\tilde{\epsilon}^p(k_z) - \lambda] \}, \quad \text{(A10)}$$

$$\tilde{t}^{sp_z} = \frac{2}{\sqrt{3}} t^{sp_z}. \quad \text{(A11)}$$

We assume that $\tilde{\boldsymbol{D}} = (\tilde{D}^{p_x}, \tilde{D}^{p_y}, 0)$ and $\tilde{\boldsymbol{M}} = (\tilde{M}^x, \tilde{M}^y, 0)$, which lie in the xy plane and are parallel to $\boldsymbol{D}$ and $\boldsymbol{M}$, respectively. It should be noted that the antisymmetric vector $\boldsymbol{D}(k_z)$ in Eq. (A7) involves the off-site hybridization t^{sp_z} and the odd-parity crystalline electric field $\tilde{\boldsymbol{D}}$ under the assumption of the strong atomic spin-orbit coupling.

Finally, we simplify the k_z dependence in Eq. (A5) as follows. For $\boldsymbol{D}(k_z)$, hereafter we retain the most interesting part, $\sin k_z$ in the numerator, for simplicity. We also drop all the k_z dependence of $\boldsymbol{M}(k_z)$. Examples of the simplified forms of $\boldsymbol{D}$ and $\boldsymbol{M}$ are found in Eqs. (17) and (18). For the dispersion in Eq. (A6), we replace it by a simple form $\epsilon(k_z) = -2t \cos k_z$ with a renormalized transfer integral t. These simplifications in Eq. (A5) lead to the effective single-band Hamiltonian for a single chain, $\mathcal{H}_{1D}^{MF}$ in Eq. (19). Finally, we obtain the effective single-band Hamiltonian $\mathcal{H}^{MF}$ in Eq. (16) by restoring the hopping term in the xy plane neglected in the derivation.

[1] P. Curie, J. Phys. Theor. Appl. **3**, 393 (1894).

[2] M. Fiebig, J. Phys. D **38**, R123 (2005).

[3] N. A. Spaldin and M. Fiebig, Science **309**, 391 (2005).

[4] W. Eerenstein, N. Mathur, and J. F. Scott, Nature (London) **442**, 759 (2006).

[5] T. Kimura, T. Goto, H. Shintani, K. Ishizaka, T. Arima, and Y. Tokura, Nature (London) **426**, 55 (2003).

[6] J. Wang, J. B. Neaton, H. Zheng, V. Nagarajan, S. B. Ogale, B. Liu, D. Viehland, V. Vaithyanathan, D. G. Schlom, U. V. Waghmare *et al.*, Science **299**, 1719 (2003).

[7] N. Hur, S. Park, P. Sharma, J. Ahn, S. Guha, and S. Cheong, Nature (London) **429**, 392 (2004).

[8] H. Katsura, N. Nagaosa, and A. V. Balatsky, Phys. Rev. Lett. **95**, 057205 (2005).

[9] M. Mostovoy, Phys. Rev. Lett. **96**, 067601 (2006).

[10] I. A. Sergienko and E. Dagotto, Phys. Rev. B **73**, 094434 (2006).

[11] T. Arima, J. Phys. Soc. Jpn. **80**, 052001 (2011).

[12] J. Scott, Nat. Mater. **6**, 256 (2007).

[13] R. Ramesh and N. A. Spaldin, Nat. Mater. **6**, 21 (2007).

[14] Y.-H. Chu, L. W. Martin, M. B. Holcomb, M. Gajek, S.-J. Han, Q. He, N. Balke, C.-H. Yang, D. Lee, W. Hu, *et al.*, Nat. Mater. **7**, 478 (2008).

[15] D. Khomskii, Physics **2**, 20 (2009).

[16] A. P. Pyatakov and A. K. Zvezdin, Phys. Usp. **55**, 557 (2012).

[17] I. B. Zel'dovich, Sov. Phys. J. Exp. Theor. Phys. **6**, 1184 (1958).

[18] A. Gorbatsevich and Y. V. Kopaev, Ferroelectrics **161**, 321 (1994).

[19] Y. F. Popov, A. Kadomtseva, G. Vorob'ev, V. Timofeeva, D. Ustinin, A. Zvezdin, and M. Tegeranchi, J. Exp. Theor. Phys. **87**, 146 (1998).

[20] H. Schmid, Ferroelectrics **252**, 41 (2001).

[21] C. Ederer and N. A. Spaldin, Phys. Rev. B **76**, 214404 (2007).

[22] N. A. Spaldin, M. Fiebig, and M. Mostovoy, J. Phys.: Condens. Matter **20**, 434203 (2008).

[23] Y. V. Kopaev, Phys. Usp. **52**, 1111 (2009).

[24] S. Miyahara and N. Furukawa, J. Phys. Soc. Jpn. **81**, 023712 (2012).

[25] V. J. Folen, G. T. Rado, and E. W. Stalder, Phys. Rev. Lett. **6**, 607 (1961).

[26] Y. F. Popov, A. Kadomtseva, D. Belov, G. Vorob'ev, and A. Zvezdin, J. Exp. Theor. Phys. Lett. **69**, 330 (1999).

[27] T. Arima, J.-H. Jung, M. Matsubara, M. Kubota, J.-P. He, Y. Kaneko, and Y. Tokura, J. Phys. Soc. Jpn. **74**, 1419 (2005).

[28] B. B. Van Aken, J.-P. Rivera, H. Schmid, and M. Fiebig, Nature (London) **449**, 702 (2007).

[29] P. Toledano, D. D. Khalyavin, and L. C. Chapon, Phys. Rev. B **84**, 094421 (2011).

[30] Y. Yanase, J. Phys. Soc. Jpn. **83**, 014703 (2014).

[31] J. D. Jackson, *Classical Electrodynamics* 3rd ed. (John Wiley and Sons, New York, 1999).

[32] J. M. Blatt and V. F. Weisskopf, *Theoretical Nuclear Physics* (Dover Publications, New York, 1991).

[33] H. Kusunose, J. Phys. Soc. Jpn. **77**, 064710 (2008).

[34] L. D. Landau and E. M. Lifshitz, *The Classical Theory of Fields*, 4th ed., Course of Theoretical Physics Vol. II (Butterworth-Heinemann, Oxford, 1980).

[35] V. Dubovik and V. Tugushev, Phys. Rep. **187**, 145 (1990).

[36] S. A. M. Mentink, A. Drost, G. J. Nieuwenhuys, E. Frikkee, A. A. Menovsky, and J. A. Mydosh, Phys. Rev. Lett. **73**, 1031 (1994).

[37] B. Volkov, A. Gorbatsevich, Y. V. Kopaev, and V. Tugushev, Zh. Eksp. Teor. Fiz **81**, 742 (1981).

[38] X. Li, T. Cao, Q. Niu, J. Shi, and J. Feng, Proc. Natl. Acad. Sci. USA **110**, 3738 (2013).

[39] C. W. Searle and S. T. Wang, Can. J. Phys. **47**, 2703 (1969).

[40] Y. Tokura, A. Urushibara, Y. Moritomo, T. Arima, A. Asamitsu, G. Kido, and N. Furukawa, J. Phys. Soc. Jpn. **63**, 3931 (1994).

[41] T. Kaplan and S. Mahanti, *Physics of Manganites* (Kluwer Academic/Plenum, New York, 1999).

[42] Y. Tokura, *Colossal Magnetoresistive Oxides* (Gordon & Breach Science Publishers, New York, 1999).

[43] A. Oyamada, M. Kondo, K. Fukuoka, T. Itou, S. Maegawa, D. X. Li, and Y. Haga, J. Phys: Condens. Matter **19**, 145246 (2007).

[44] Y. Yanase and H. Harima (private communication).